

University of Dundee

## Oblique impact breakage unification of nonspherical particles using discrete element method

Peng, Di; Wang, Li Ge; Lin, Yuquan; Zhu, Chongqiang; Chen, Xizhong; Liu, Zhihui

*Published in:*  
Particuology

*DOI:*  
[10.1016/j.partic.2023.11.012](https://doi.org/10.1016/j.partic.2023.11.012)

*Publication date:*  
2024

*Licence:*  
CC BY

*Document Version*  
Publisher's PDF, also known as Version of record

[Link to publication in Discovery Research Portal](#)

### *Citation for published version (APA):*

Peng, D., Wang, L. G., Lin, Y., Zhu, C., Chen, X., Liu, Z., & Ge, R. (2024). Oblique impact breakage unification of nonspherical particles using discrete element method. *Particuology*, 90, 61-71. Advance online publication. <https://doi.org/10.1016/j.partic.2023.11.012>

### **General rights**

Copyright and moral rights for the publications made accessible in Discovery Research Portal are retained by the authors and/or other copyright owners and it is a condition of accessing publications that users recognise and abide by the legal requirements associated with these rights.

### **Take down policy**

If you believe that this document breaches copyright please contact us providing details, and we will remove access to the work immediately and investigate your claim.



# Oblique impact breakage unification of nonspherical particles using discrete element method



Di Peng<sup>a, b, c</sup>, LiGe Wang<sup>a, d</sup>, Yuquan Lin<sup>e, f</sup>, Chongqiang Zhu<sup>e, g</sup>, Xizhong Chen<sup>h</sup>,  
Zhihui Liu<sup>d, \*\*</sup>, Ruihuan Ge<sup>i, \*</sup>

<sup>a</sup> Shenzhen Research Institute of Shandong University, Shenzhen 518057, China

<sup>b</sup> Institute of Foundation Engineering, China Academy of Building Research, Beijing 100013, China

<sup>c</sup> Ubiquitous Particle Ltd., Twickenham, London TW2 7AU, UK

<sup>d</sup> Department of Smart Manufacturing and Engineering Software, School of Qilu Transportation, Shandong University, Jinan 250061, China

<sup>e</sup> Department of Geotechnical Engineering, Tongji University, Shanghai 200092, China

<sup>f</sup> School of Transportation and Civil Engineering, Shandong Jiaotong University, Jinan 250357, China

<sup>g</sup> School of Science and Engineering, University of Dundee, Dundee DD1 4HN, UK

<sup>h</sup> Department of Chemical Engineering, School of Chemistry and Chemical Engineering, Shanghai Jiao Tong University, Shanghai 200240, China

<sup>i</sup> Department of Chemical and Biological Engineering, University of Sheffield, Sheffield S1 3JD, UK

## ARTICLE INFO

### Article history:

Received 18 June 2023

Received in revised form

15 October 2023

Accepted 1 November 2023

Available online 25 November 2023

### Keywords:

Breakage master curve

Nonspherical particle

Oblique impact

Equivalent velocity

Discrete element method (DEM)

Bonded contact model

## ABSTRACT

Particle breakage commonly occurs during processing of particulate materials, but a mechanistic model of particle impact breakage is not fully established. This article presents oblique impact breakage characteristics of nonspherical particles using discrete element method (DEM) simulations. Three different particle shapes, i.e. spherical, cuboidal and cylindrical, are investigated. Constituent spheres are agglomerated with bridging bonds to model the breakage characteristics under impact conditions. The effect of agglomerate shapes on the breakage pattern, damage ratio, and fragment size distribution is fully investigated. By using a newly proposed oblique impact model, unified breakage master surfaces are theoretically constructed for all the particle shapes under oblique impact conditions. The developed approach can be applied to modelling particulate processes where nonspherical particles and oblique impact breakage are prevailing.

© 2023 Chinese Society of Particuology and Institute of Process Engineering, Chinese Academy of Sciences. Published by Elsevier B.V. This is an open access article under the CC BY license (<http://creativecommons.org/licenses/by/4.0/>).

## 1. Introduction

Particle impact breakage is commonly encountered in typical particulate processes such as milling, pneumatic conveying (Wang, Ge, et al., 2021). The mechanistic-based systematic description of particle impact breakage is highly desirable but is not yet fully established. This is mainly because of complicated stressing conditions, varied particle properties and empiricism of breakage models. Experimental studies of particle impact breakage were first conducted in early stages and have been widely reported by numerous researchers in the literature (Cheong et al., 2003; Qin et al., 2023; Salman et al., 1995; Subero & Ghadiri, 2001; Yuregir et al., 1986). The focal point of these research is identification of

influential breakage parameters and distinction of breakage pattern regarding the impact conditions (Subero & Ghadiri, 2001). The influential parameters of impact breakage can be summarized as internal properties such as binding mechanism and structure (Ge et al., 2018), physical properties such as size and shape (Liu et al., 2010; Thornton & Liu, 2004), mechanical properties such as hardness and fracture toughness (Wang, Chen, & Ooi, 2021), statistical properties such as varied particle strength of primary particles (Orozco et al., 2019), impact target (Ye et al., 2021), and impact conditions such as impact velocity, impact number and impact angle (Salman et al., 1995; Wang et al., 2022). Despite significant insights from the above studies, a major shortcoming from the experiments is the post-mortem analysis of impact breakage information such as particle size distribution. The short duration of impact breakage presents a huge challenge for experimental apparatus to fully capture the contact behaviour between particles and the impact target. Even with the aid of high-speed recording

\* Corresponding author.

\*\* Corresponding author.

E-mail addresses: [Zhihui.liu@sdu.edu.cn](mailto:Zhihui.liu@sdu.edu.cn) (Z. Liu), [ruihuan.ge@gmail.com](mailto:ruihuan.ge@gmail.com) (R. Ge).

Nomenclature			
$a$	Major half-axis length (m)	$S_C$	Mean compressive strength (MPa)
$A_b$	Section area of the bond (m <sup>2</sup> )	$S_S$	Mean shear strength (MPa)
$b$	Moderate half-axis length (m)	$S_T$	Mean tensile strength (MPa)
$B$	Breakage ratio	$\mathbf{u}$	Bond side displacement/rotation vector
$c$	Minor half-axis length (m)	$v_r$	Reference velocity (m/s)
$d$	Diameter (m)	$V$	Total particle volume (m <sup>3</sup> )
$D$	Damage ratio	<i>Greek symbols</i>	
$D_C$	Standard variation of compressive strength (Pa)	$\alpha$	Constant
$D_S$	Standard variation of shear strength (Pa)	$\beta$	Intermediate parameter
$D_T$	Standard variation of tensile strength (Pa)	$\gamma$	Velocity normalisation factor (m/s)
$e_{rp}$	Particle–particle restitution	$\zeta_p$	Scaling factor for constituent sphere
$e_{pg}$	Particle–geometry coefficient of restitution	$\zeta_c$	Contact radius multiplier for constituent sphere
$E_b$	Bond Young's modulus (Pa)	$\theta$	Impact angle (rad)
$E_p$	Particle Young's modulus (Pa)	$\lambda$	Bond radius multiplier
$E_g$	Geometry Young's modulus (Pa)	$\mu_{sp}$	Particle–particle static friction
$\mathbf{F}$	Bond side force/moment vector	$\mu_{rp}$	Particle–particle rolling friction
$I_b$	Bond section moment of inertia (m <sup>4</sup> )	$\mu_{sg}$	Particle–geometry coefficient of static friction
$\mathbf{K}$	Bond stiffness matrix	$\mu_{rg}$	Particle–geometry coefficient of rolling friction
$l$	Cylinder length (m)	$\nu_b$	Poisson's ratio
$L_b$	Bond length (m)	$\nu_p$	Particle Poisson's ratio
$L_e$	Cube edge length (m)	$\nu_g$	Geometry Poisson's ratio
$m$	Velocity exponent	$\Phi$	Timoshenko beam stiffness factor
$n_b$	Total number of bonds	$\rho_p$	Particle density (kg/m <sup>3</sup> )
$n_c$	Average coordination number	$\sigma_c$	Bond compressive strength (Pa)
$n_p$	Total number of constituent spheres	$\sigma_t$	Bond tensile strength (Pa)
$p$	Porosity	$\tau$	Bond shear strength (Pa)
$r_b$	Bond radius (m)	$\xi$	Tangential contribution factor

system, the identification of impact site and the crack propagation through internal structure of particles is still not possible. In a nutshell, very little insight into the dynamics of breakage process can be provided solely from the experimental means. Only recently Ge et al. proposed a new 3D printed test particle approach that could experimentally investigate the particle breakage characteristics under highly controllable conditions (Ge et al., 2017, 2018).

In view of the experimental limitations, computational techniques, such as Monte Carlo method (Mishra, 2000), Discrete Element Method (DEM) (Chen et al., 2021; Ge et al., 2019, 2020; Shang, 2022) and Finite Element Method (FEM) (Kh et al., 2011) have been generally accepted as powerful tools for particle impact breakage. Amongst these methods, DEM which describes the relationships between microscopic and macroscopic properties renders impact breakage with both scientific and industrial interests. This is due to the fact that DEM is able to consider the shapes and properties of individual particles and forces acting on them (Zeng et al., 2019; Zheng et al., 2015). Therefore, probing the breakage of a single particle using DEM becomes essential towards a systematic understanding of particulate system behaviour spanning from geotechnical, through mineral (Wang et al., 2022) and chemical (Moreno-Atanasio & Ghadiri, 2006) to pharmaceutical engineering (Chen et al., 2020). In the context of DEM, particle impact breakage is often simulated using cohesive or rigid bonded particle model. A large number of this kind of study on particle impact breakage using DEM can be found in the literature (Kafui & Thornton, 2000; Thornton & Liu, 2004; Wang et al., 2022). The key findings from DEM-based particle impact breakage include but are not limited to the following highlights: 1) The damage ratio (the proportion of broken inter-particle bonds) is increased with the increase of impact velocity (Wang et al., 2022). 2) The breakage pattern can be transmitted from disintegration to fragmentation by

increasing the contact density or changing the agglomerate surface (Wang et al., 2022). Alternative DEM methods lie in replacing parent particles by smaller ones once failure criterion is met over the impact process and fast-breakage model using Laguerre\_voronoi tessellation to segment the particle in 2D polygons or 3D polyhedral (Monteiro et al., 2015). A comprehensive assessment of these three methods was performed whereas more details can be found elsewhere (Jiménez-Herrera et al., 2018). Nevertheless, the above-mentioned DEM studies of particle impact breakage were predominantly carried out under normal impact for spherical particles. However, the particles agglomerated through the granulation process are not ideally spherical and hence the collision behaviour of nonspherical particles is much more different from that of spherical particles (Liu et al., 2010). Moreover, the impact angle is not expected to be always normal and oblique impact is understood to be prevailing in a wide spectrum of particulate system behaviour.

There have been a few DEM studies of impact breakage for nonspherical particles. For example, a DEM study of agglomerate impact breakage was carried out considering three shapes, i.e. spherical, cuboidal and cylindrical (Liu et al., 2010). It was found that internal damage of particle is closely tied to the particle deceleration adjacent to the impact site. Nevertheless, the breakage mode for nonspherical agglomerates is not decisively dependent on the local microstructure (Liu et al., 2010). Another example of impact breakage for six particle shapes including spherical, regular tetrahedral, cuboidal, regular octahedron, regular dodecahedron and regular icosahedrons was reported in the DEM simulations by Zheng et al. (Zheng et al., 2015). They found that the size of contact area plays a key role in particle breakage. The maximum target force and final damage ratio decreases when the face-impact, edge-impact and vertex-impact modes are applied. Minor changes in

particle sphericity give rise to remarkable different breakage patterns for nonspherical particles. Further DEM study of ellipsoidal particle impact breakage was carried out to probe the effect of impact velocity and moisture content through the parallel bond models (Zeng et al., 2019). The effect of moisture content on ellipsoid particle breakage relies on the impact velocity, showing the damage ratio increases linearly whilst the size ratio of the largest fragment decreases linearly for the local disintegration mode.

This article presents an innovative approach to establish a unified breakage master curve for nonspherical particles under various impact velocities and impact angles. The oblique impact breakage of three shaped particles, i.e. cubical, cylindrical, ellipsoidal is carried out using a DEM bond contact model. The micromechanical-based damage ratio, which is conventionally used in DEM as a function of number of bonds is converted as macroscopic breakage ratio as a function of fragment size distribution. The conversion from damage ratio to breakage ratio is enabled by implementing a Breadth-First Search algorithm. A recently developed oblique impact model considering the effect of impact angle is extended to construct unified breakage master curve for nonspherical particle impact breakage.

## 2. Particle breakage model in DEM

In this study, the interparticle bond contact model is adopted for modelling particle breakage. Constituent spheres are bonded to form an agglomerate, which represents the particle for breakage in DEM simulation. The bond contact model adopted in this study is Edinburgh bonded particle model (EBPM). EBPM was initially developed by Brown et al. (Brown et al., 2014) and implemented as an API plugin in commercial DEM code EDEM afterwards. EBPM performs the mechanical behaviour of bond between two neighbouring particles with a tiny gap (Fig. 1). The bond acts as a Timoshenko beam mechanically after generation, linking the centres of the two particles at its both sides. The mechanical act of the contact is described as follows:

$$\Delta \mathbf{F} = \mathbf{K} \Delta \mathbf{u} \quad (1)$$

where,  $a, b$  represent the two sides of the bond,  $\Delta \mathbf{F}$  represents the collection of force/moment incrementations at both sides of the bond,  $\Delta \mathbf{u}$  represents the collection of displacement/rotation

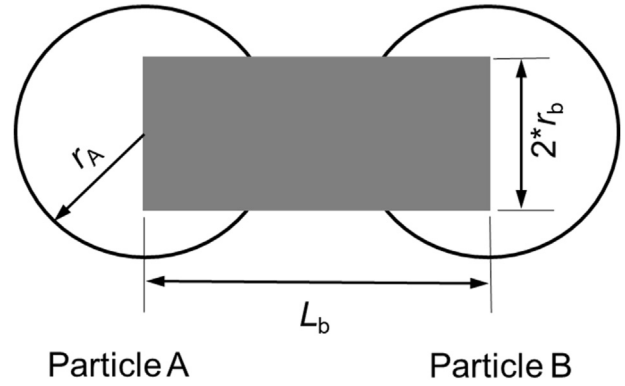


Fig. 1. Illustration of the bond of Edinburgh bonded particle model (EBPM) (particle radius  $r_A$ , bond length  $L_b$ , bond radius  $r_b$ ) (Ge et al., 2020; Yang et al., 2023).

incrementations at both sides of the bond,  $\mathbf{K}$  represents the stiffness matrix, in which the stiffness parameters  $k_1 = \frac{E_b A_b}{L_b}$ ,  $k_2 = \frac{12 E_b I_b}{L_b^3 (1 + \Phi)}$ ,  $k_3 = \frac{6 E_b I_b}{L_b^2 (1 + \Phi)}$ ,  $k_4 = \frac{E_b I_b}{L_b (1 + \nu_b)}$ ,  $k_5 = \frac{E_b I_b (4 + \Phi)}{L_b (1 + \Phi)}$ ,  $k_6 = \frac{E_b I_b (2 - \Phi)}{L_b (1 + \Phi)}$ , contact area  $A_b = \pi r_b^2$ , contact section moment of inertia  $I_b = \frac{\pi r_b^4}{4}$ , Timoshenko beam parameter  $\Phi = \frac{20 r_b^2 (1 + \nu_b)}{3 L_b^2}$ , bond radius  $r_b = \eta \min(r_1, r_2)$ ,  $E_b$  and  $\nu_b$  are bond Young's modulus and Poisson's ratio, respectively,  $\eta$  is bond radius multiplier,  $r_1, r_2$  are the radii of the two bonding spheres, respectively.

The bond will fail as its stress exceeds the strength in the corresponding direction, after which the bond contact will switch to Hertz–Mindlin granular contact. The bond failure criteria are as follows:

$$\sigma_i = \frac{F_{bx}}{A_b} - \frac{r_b \sqrt{M_{iy}^2 + M_{iz}^2}}{I_b}, i = a, b \quad (5)$$

$$\sigma_c = \min(\sigma_a, \sigma_b) \leq -[\sigma_c] \quad (6)$$

$$\sigma_t = \max(\sigma_a, \sigma_b) \geq [\sigma_t] \quad (7)$$

$$\mathbf{K} = \begin{bmatrix} k_1 & 0 & 0 & 0 & 0 & 0 & -k_1 & 0 & 0 & 0 & 0 & 0 \\ 0 & k_2 & 0 & 0 & 0 & k_3 & 0 & -k_2 & 0 & 0 & 0 & k_3 \\ 0 & 0 & k_2 & 0 & -k_3 & 0 & 0 & 0 & -k_2 & 0 & -k_3 & 0 \\ 0 & 0 & 0 & k_4 & 0 & 0 & 0 & 0 & 0 & -k_4 & 0 & 0 \\ 0 & 0 & -k_3 & 0 & k_5 & 0 & 0 & 0 & k_3 & 0 & k_6 & 0 \\ 0 & k_3 & 0 & 0 & 0 & k_5 & 0 & -k_3 & 0 & 0 & 0 & k_6 \\ -k_1 & 0 & 0 & 0 & 0 & 0 & k_1 & 0 & 0 & 0 & 0 & 0 \\ 0 & -k_2 & 0 & 0 & 0 & -k_3 & 0 & k_2 & 0 & 0 & 0 & -k_3 \\ 0 & 0 & -k_2 & 0 & k_3 & 0 & 0 & 0 & k_2 & 0 & k_3 & 0 \\ 0 & 0 & 0 & -k_4 & 0 & 0 & 0 & 0 & 0 & k_4 & 0 & 0 \\ 0 & 0 & -k_3 & 0 & k_6 & 0 & 0 & 0 & k_3 & 0 & k_5 & 0 \\ 0 & k_3 & 0 & 0 & 0 & k_6 & 0 & -k_3 & 0 & 0 & 0 & k_5 \end{bmatrix} \quad (2)$$

$$\Delta \mathbf{F} = [\Delta F_{ax} \quad \Delta F_{ay} \quad \Delta F_{az} \quad \Delta M_{ax} \quad \Delta M_{ay} \quad \Delta M_{az} \quad \Delta F_{bx} \quad \Delta F_{by} \quad \Delta F_{bz} \quad \Delta M_{bx} \quad \Delta M_{by} \quad \Delta M_{bz}]^T \quad (3)$$

$$\Delta \mathbf{u} = [\Delta d_{ax} \quad \Delta d_{ay} \quad \Delta d_{az} \quad \Delta \theta_{ax} \quad \Delta \theta_{ay} \quad \Delta \theta_{az} \quad \Delta d_{bx} \quad \Delta d_{by} \quad \Delta d_{bz} \quad \Delta \theta_{bx} \quad \Delta \theta_{by} \quad \Delta \theta_{bz}]^T \quad (4)$$

$$\tau = \frac{|M_{ax}|r_b}{2I_b} + \frac{4\sqrt{F_{ay}^2 + F_{az}^2}}{3A_b} \geq [\tau] \quad (8)$$

where,  $\sigma_c, \sigma_t, \tau$  are compressive, tensile and shear stresses of the bond, respectively, and  $[\sigma_c], [\sigma_t], [\tau]$  are compressive, tensile, and shear strengths of the bond, respectively.

### 3. Particle assembly and DEM simulation setup

#### 3.1. Nonspherical particle assembly

Nonspherical particles can be performed using a variety of descriptors. Multisphere clump is a conventional descriptor. A multisphere clump contains several rigidly composed spheres, based on which all interparticle contacts are processed. The whole clump is one particle when dealing with particle motion though. There are also ellipsoidal clumps and even superellipsoidal clumps available in these DEM codes (DCS Computing GmbH, 2020; Liu et al., 2021). Another multielemental descriptor is bonded sphere series in which spheres are all bonded into an agglomerate and the agglomerate describes the particle. This descriptor has the advantage of revealing micro mechanical behaviour of particle breakage with the mechanical evolution of bonds between the constituent spheres. In this article, this descriptor is adopted. Despite multielemental descriptors, there are continuous function representation (CFR) and discrete function representation (DFR) describing the surface of particles (Lu et al., 2015). CFR describes particle surface with a continuous function and a specific contact detection algorithm needs to be developed to resolve the (non-)contact between particles, whilst DFR describes particle surface with a set of points base on which contact detection can be conducted. There are many types of nonspherical particles based on CFR descriptor. Polyhedra can be one type of CFR nonspherical particles with several facets, and superellipsoids (Podlozhnyuk et al., 2017) can be another type of CFR nonspherical particles. There are also other continuous functional surfaced particles (Andrade et al., 2012; Capozza & Hanley, 2021). It is noted that there are some differences on bulk mechanical behaviour when using different nonspherical particle descriptors such as multisphere clumps and superquadrics (Soltanbeigi et al., 2018, 2021).

In this article, the nonspherical particle is assembled by bonding an amount of constituent spheres. Three shapes of the nonspherical particles are considered: cube, cylinder, ellipsoid. These can all be described as superellipsoids, with different roundness parameters (see superquadrics in (Lu et al., 2015), superellipsoids are included in superquadrics). Superellipsoid with the first roundness  $\varepsilon_1 \rightarrow 0^+$  and the second roundness  $\varepsilon_2 \rightarrow 0^+$  refers to a quasi-cube. Superellipsoid with the first roundness  $\varepsilon_1 = 1.0$  and the second roundness  $\varepsilon_2 \rightarrow 0^+$  refers to a quasi-cylinder. Superquadric with the two roundness parameters  $\varepsilon_1 = \varepsilon_2 = 1.0$  refers to an ellipsoid. Our previous study adopted a spherical particle with a 50 mm radius for breakage study (Wang et al., 2022). The three shapes in this study keep the volume consistent to the spherical particle. Therefore, the size of the three shapes can be derived. It is noted that for cylinder, the length equals to the diameter, and for ellipsoid, the major aspect ratio  $a/b = 2.0$  whilst the minor aspect ratio  $b/c = 1.0$ . Then, constituent spheres are filled into the particle space. The size distribution and filling method of constituent spheres keep the same as those in previous study (Wang et al., 2022). Fig. 2 shows the size distribution of constituent spheres. Particle scaling (Thakur et al., 2016) is introduced in this study with the scaling factor of 1.15. This allows fewer constituent spheres within the simulation and thus accelerate the DEM simulation. In addition, the contact radius

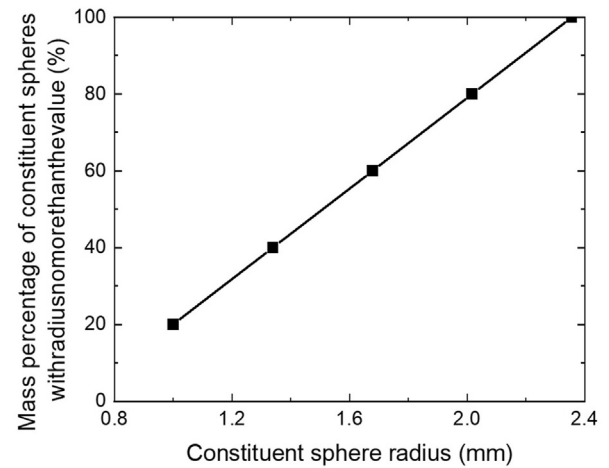


Fig. 2. Size distribution of constituent spheres.

of the constituent spheres is set to 1.1 multiplying scaled radius, to provide a reference gap of 10% within which the other constituent sphere will be bonded. Following this principle, all the bonds are generated. The size parameters of the three shapes are listed in Table 1 in which the number of bonds can be found, along with other size parameters mentioned above. The assembled nonspherical agglomerates are illustrated in Fig. 3. The average coordination number is between 6.8–7 for all types of nonspherical particles, which refers to densely bonded agglomerates.

#### 3.2. Model parameterisation

The parameters of EBPM are shown in Table 2, which are all consistent to (Brown et al., 2014; Wang et al., 2022). When the bond fails, the particle–particle contact model goes to nonslip Hertz–Mindlin model. The same model is adopted for particle–geometry contacts, but with different parameters. All these parameters are listed in Table 3 (Brown et al., 2014; Wang et al., 2022). The parameters used for EBPM have been justified in our previous work (Wang et al., 2022).

#### 3.3. Simulation setup

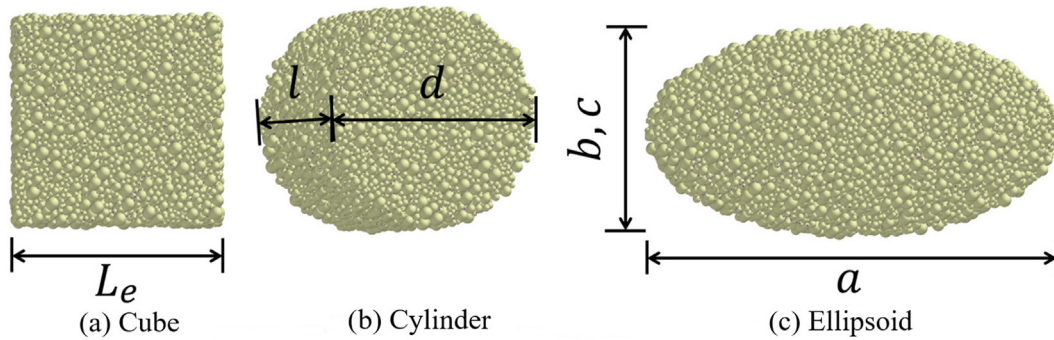
Once produced, the bonded nonspherical agglomerates are set a velocity by assigning all the constituent spheres the same velocity. The magnitude of the velocity, or the reference velocity  $v_r$ , is 5, 10, 15, 20, 25, 30, 35, 40, 45, 50 m/s, respectively. A steel plate (planar geometry) is set on which the oblique impact occurs. The direction of the velocity keeps an angle  $\theta$  to the normal vector of the plate (Fig. 4).  $\theta = 90^\circ, 75^\circ, 60^\circ, 45^\circ, 30^\circ$ , respectively. Therefore, a total number of 150 DEM simulation cases (three agglomerate shapes, ten reference velocities and five impact angles) have been performed. It is noted that no gravity is set for all the DEM simulations. The agglomerates will move until contacting steel surface and then breaking into fragments. The process of an oblique impact is then reproduced. The orientation of nonspherical particles keeps the same in orthogonal direction to maintain the same point of impact on particle surface among different simulations. Further work will be done in the future incorporating the effect of particle orientation on oblique impact.

The time step adopted in this study is  $\Delta t = 1.00 \times 10^{-7}$  s. For two nonspherical particle scenarios, Peng et al. (Peng et al., 2021) gives a critical time step calculation. Substituting EBPM bonded contact parameters, the critical time step is  $\Delta t_{cri} = 7.08 \times 10^{-7}$  s.



**Table 1**  
Characteristics of particle assembly.

Parameter	Description	Cube value	Cylinder value	Ellipsoid value
Shape-relevant parameters				
$L_e$	Edge length (m)	$8.06 \times 10^{-2}$	—	—
$d$	Diameter (m)	—	$8.74 \times 10^{-2}$	—
$l$	Length (m)	—	$8.74 \times 10^{-2}$	—
$a$	Major half-axis length (m)	—	—	$7.94 \times 10^{-2}$
$b$	Moderate half-axis length (m)	—	—	$3.97 \times 10^{-2}$
$c$	Minor half-axis length (m)	—	—	$3.97 \times 10^{-2}$
$a/b$	Major aspect ratio (—)	—	—	2.0
$b/c$	Minor aspect ratio (—)	—	—	1.0
Shape-irrelevant parameters				
$V$	Total volume (m <sup>3</sup> )	$5.24 \times 10^{-4}$	$5.24 \times 10^{-4}$	$5.24 \times 10^{-4}$
$\zeta_p$	Scaling factor for constituent sphere (—)	1.15	1.15	1.15
$\zeta_c$	Contact radius multiplier for constituent sphere (—)	1.10	1.10	1.10
$n_p$	Total number of constituent spheres (—)	18,112	18,093	18,030
$p$	Porosity (—)	0.37	0.37	0.37
$n_b$	Total number of bonds (—)	61,898	62,632	62,581
$n_c$	Average coordination number (—)	6.835	6.923	6.942

**Fig. 3.** Nonspherical agglomerates used for DEM simulation.**Table 2**  
Input value of bond parameters (Brown et al., 2014; Wang et al., 2022).

Parameter	Description	Value
$E_b$	Young's modulus (GPa)	28
$\nu_b$	Poisson's ratio (—)	0.2
$S_c$	Mean compressive strength (MPa)	300
$D_c$	Standard variation of compressive strength (MPa)	0
$S_T$	Mean tensile strength (MPa)	60
$D_T$	Standard variation of tensile strength (MPa)	0
$S_S$	Mean shear strength (MPa)	60
$D_S$	Standard variation of shear strength (MPa)	0
$\lambda$	Bond radius multiplier (—)	0.5

Considering multi contacts in the bonded agglomerates, the critical time step is shrunk to ensure stable numerical computation (Otsubo et al., 2017).

## 4. Results and discussion

### 4.1. Failure mode, force, and velocity evolution during impact

Specifically, a typical simulation case with impact velocity of 10 m/s and  $\theta = 90^\circ$  is selected for failure mode study. The bond network failure characteristics of different types of nonspherical particles are illustrated in Fig. 5. As shown in Fig. 5, cube has

**Table 3**  
Input value of non-bonded parameters (Brown et al., 2014; Wang et al., 2022).

Parameter	Description	Value
$E_p$	Particle Young's modulus (GPa)	70
$\rho_p$	Particle density (kg/m <sup>3</sup> )	2650
$\nu_p$	Particle Poisson's ratio (—)	0.25
$e_{rp}$	Particle–particle restitution (—)	0.9
$\mu_{sp}$	Particle–particle static friction (—)	0.3
$\mu_{rp}$	Particle–particle rolling friction (—)	0.01
$E_g$	Geometry Young's modulus (GPa)	200
$\nu_g$	Geometry Poisson's ratio (—)	0.25
$e_{pg}$	Particle–geometry coefficient of restitution (—)	0.7
$\mu_{sg}$	Particle–geometry coefficient of static friction (—)	0.35
$\mu_{rg}$	Particle–geometry coefficient of rolling friction (—)	0.01

fractured during post-breakage process, but the fracture is later than the local crush on the impact surface. Cylinder has a similar breakage mechanism as spherical agglomerate in previous study (Wang et al., 2022), with a fracture through the agglomerate along with localised crushes on the impact surface. Multiple fragments could be observed when  $t = 0.01$ s. Ellipsoid does not have a crack through the whole impact process. The difference between ellipsoid and other two shapes is that it contains inhomogeneity, and the direction of impact for ellipsoid is its major axis of scale. As the

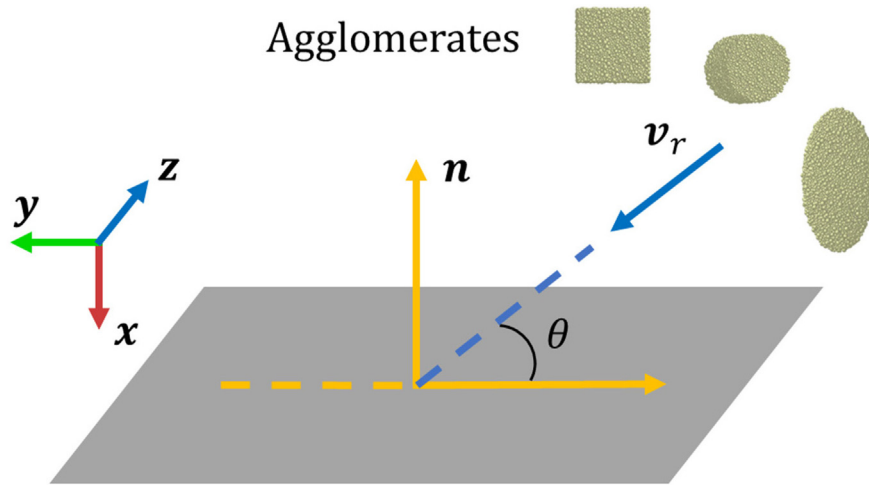


Fig. 4. Illustration of the oblique impact breakage setup.

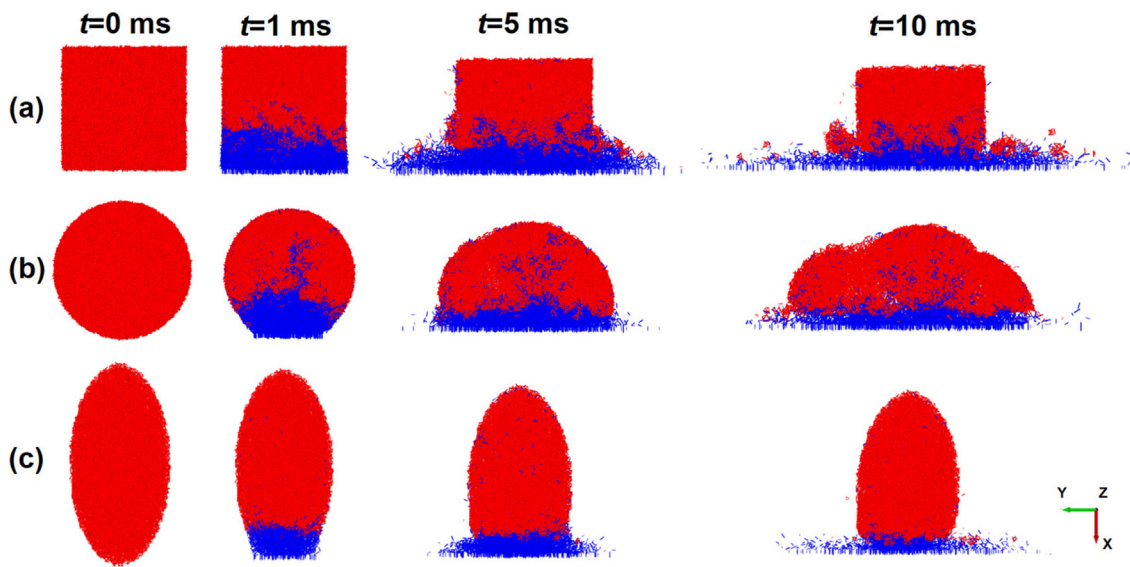


Fig. 5. Surface damage resulting in localised damage at impact velocity of 10 m/s and  $\theta = 90^\circ$ . (a) Cube (b) Cylinder (c) Ellipsoid (red = intact bond, blue = broken bond).

major axis has the largest resistance towards fracture failure, only local crush can be observed.

Fig. 6 shows the velocity evolution of these impacts. For cube and cylinder with fractures, the regions of constituent spheres with reduced velocities are the same as those with fracture and local crush. Constituent spheres with large velocity difference transfer large kinematic energy into bonds, and thus cause bond failure in micro and fracture and local crush in macro. In the post-failure stage, the spheres spread backwards the agglomerate, with the velocity half of the initial. More than 3/4 of the initial kinematic energy of these spheres is dissipated. For ellipsoid without fracture, constituent spheres in local crush region also experience large velocity drop, but in post-failure stage small number of spheres spread with similar velocity to initial while large number of spheres are close to stop. The agglomerate with fractures has larger coefficient of restitution, due to different level of resistance provided by micro bonds. The results in Figs. 5 and 6 show the effect of particle shape, especially the shape relevant to the impact surface could significantly affect the breakage patterns.

#### 4.2. Influence of impact orientation and tangential velocity

Fig. 7 shows the velocity field of constituent spheres within three types of agglomerates with impact angle  $\theta = 90^\circ, 60^\circ, 30^\circ$ , while the reference velocity keeps the same as  $v_r = 10$  m/s. The local crush decreases when the angle of impact  $\theta$  increases, as normal impact velocity  $v_n = v_r \sin \theta$  decreases with  $\theta$  and the local crush is mainly induced by normal impact. The region of constituent sphere spread is linked to the impulse energy of impact and shrinks as  $\theta$  increases due to the decrease of normal impact velocity.

#### 4.3. Damage ratio analysis

Fig. 8 shows the damage ratios  $D$  for the three types of shapes with all impact velocities and angles. Here, the damage ratio is defined as the number of broken bonded contacts over the number of total bonded contacts and should be from 0 to 1. The damage ratio increases with impact velocity due to the increase of kinematic energy charging to the bonds during oblique impact.

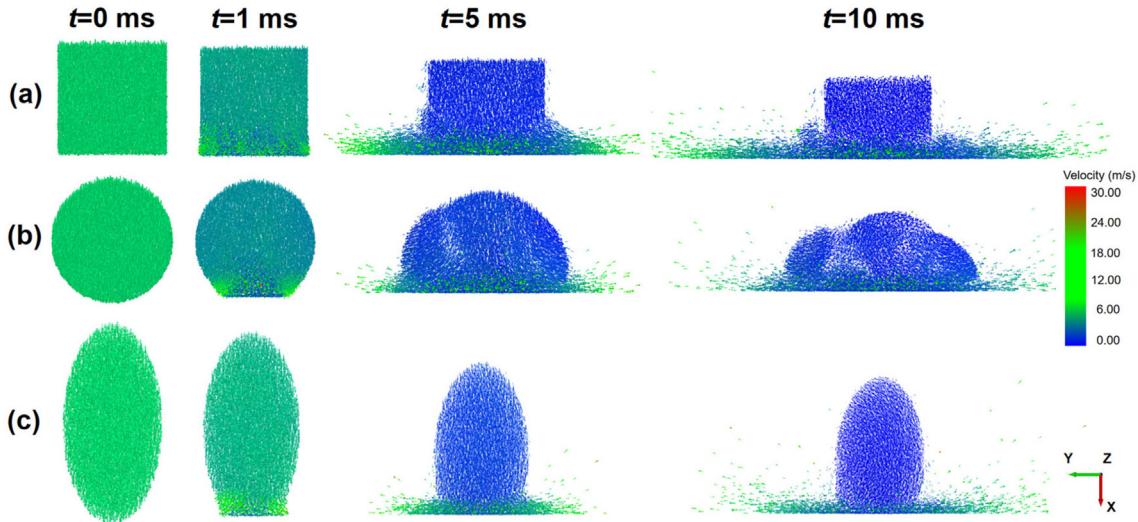


Fig. 6. Velocity field of constituent spheres at impact velocity of 10 m/s and  $\theta = 90^\circ$ . (a) Cube (b) Cylinder (c) Ellipsoid.

The damage ratio decreases with impact angle. This is due to the decrease of normal velocity to the surface of impact, showing that the normal direction is the major direction causing bond failure. Cube and cylinder have similar damage ratios during impact, as the two surfaces representing cube and cylinder in Fig. 7(b) intersect with each other; ellipsoid has apparently lower damage ratio compared to the other shapes, as the surface representing ellipsoid in Fig. 7(a) is apparently apart from the other two surfaces. This further indicates the effect of shape on the breakage characteristics.

#### 4.4. Fragment size distribution and breakage ratio

During post-breakage, the size distribution of fragments from the original agglomerate differs from the one of constituent spheres, as there will be bonds remaining in the fragments. Size distribution analysis is therefore essential. A Breadth-First search algorithm is used to analyse the fragment size distribution of particle assemblies. Firstly, each contact is assigned an ID. At each iteration the algorithm can be used to check if a new ID belonging to an existing particle cluster. An individual particle cluster could be identified by checking through all the particles in contact. In this way, all the fragments within a particle assembly could be identified. Afterwards shape fitting function is used to analyse the fragment size distribution. Each fragment is assumed to have an ellipsoidal shape for simplification. The size is calculated using the following function:

$$d = \beta \sqrt{0.5(1 + \alpha^2)} \quad (9)$$

where,  $d$  is the calculated fragment size,  $\beta$  is the intermediate diameter, and  $\alpha = 0.9$  is a constant between the shortest and intermediate diameter of an ellipsoid. Detailed descriptions of Breadth-First search algorithm and shape fitting approach are given in our previous work (Wang et al., 2022).

Fig. 9 shows the particle size distribution (PSD) of the fragments at the final stage of the impact. Fig. 9(a) shows the PSD of impacts with same impact velocity  $v_r = 10$  m/s. The curve can be separated into two series: for cube and cylinder with impact angle  $\theta \geq 60^\circ$ , the PSD tends to be flatter, indicating that the original agglomerate was segmented to several major blocks; for cube and cylinder with impact angle  $\theta = 30^\circ$  and ellipsoid with all impact angles, the PSD

experiences a sudden increase caused by the unbroken part of the original agglomerate, indicating that only small fragments were generated. This result corresponds to the failure of agglomerates that is shown in Fig. 5. Fig. 9(b) shows the PSD of impacts with same impact angle  $\theta = 90^\circ$ . For all types of shapes, the amount of fragments generated increases apparently with impact velocity, due to the increase of impulse energy during impact; cube and cylinder have similar PSDs for all impact velocities, while ellipsoid generates fewer fragments compared with cube and cylinder with the same impact velocity. All the PSD curves in both Fig. 9(a) and (b) have expressed a low slope at the left and a huge increase at the right, referring to small fragments and the largest mother fragment, respectively. This corresponds to the experimental results (Subero & Ghadiri, 2001; Wang et al., 2022) and numerical results in previous study (Wang et al., 2022).

#### 4.5. An oblique impact model and unified breakage master surface

An oblique impact breakage model developed in our previous work (Wang et al., 2022) is adopted to unify the oblique impact of agglomerates. An equivalent velocity  $v_{eq}$  is proposed by Wang et al. (Wang et al., 2022) that can take the velocity tangential component into account:

$$v_{eq} = v_r \sqrt{\sin^2 \theta + \xi \sin^2 \theta \cos^2 \theta} \quad (10)$$

In this expression,  $v_r$  is impact velocity magnitude (m/s),  $\theta$  is angle of impact ( $^\circ$ ),  $\xi$  is tangential contribution factor ( $-$ ).

To describe the breakage ratio  $B$  of fragmentation under impact loading, the Weibull distribution is used:

$$B = 1 - \exp \left[ - \left( \frac{v_{eq}}{\gamma} \right)^m \right] \quad (11)$$

where,  $m$  and  $c$  are fitting parameters ( $-$ ). Substituting Eq. (10) into Eq. (11), it evolves

$$B = 1 - \exp \left[ - \left( \frac{v_r}{\gamma} \sqrt{\sin^2 \theta + \xi \sin^2 \theta \cos^2 \theta} \right)^m \right] \quad (12)$$

In this expression, the tangential contribution factor  $\xi$ , the velocity normalisation factor  $\gamma$  and the velocity exponent  $m$  are model parameters and need to be fitted.



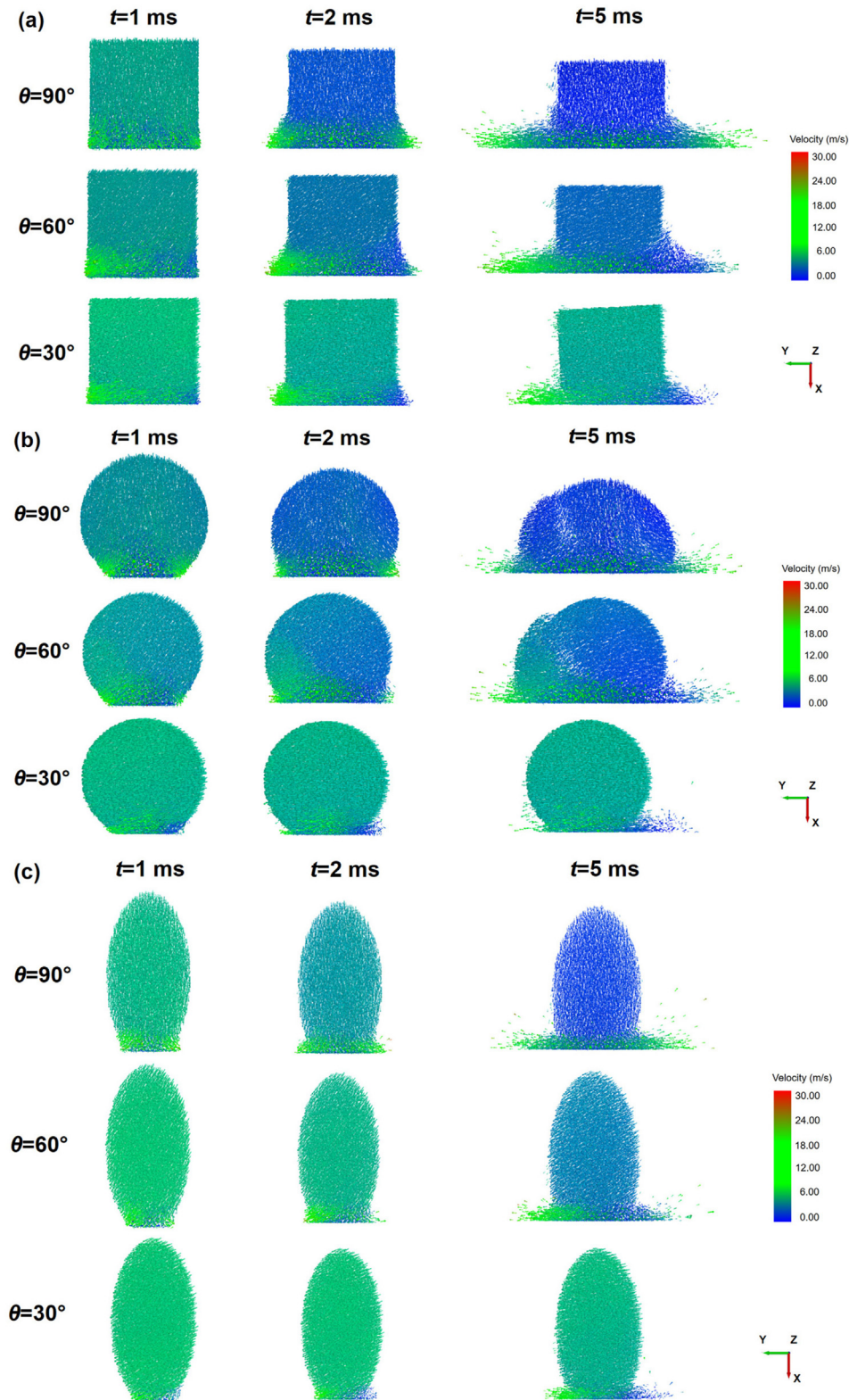


**Fig. 7.** Spatial distribution of particle velocity under different impact angles under 10 m/s impact. (a) Cube (b) Cylinder (c) Ellipsoid.

Fig. 10 shows the unified breakage master surface for breakage ratio of three types of agglomerates. The surface is fitted using the Levenberg–Marquardt algorithm (Moré, 2006), an advance of

Gaussian Newton iteration method, with Eq. (12) as expression. Table 4 shows the corresponding fitting parameters in Fig. 10. As mentioned above, all these three types of shapes belong to

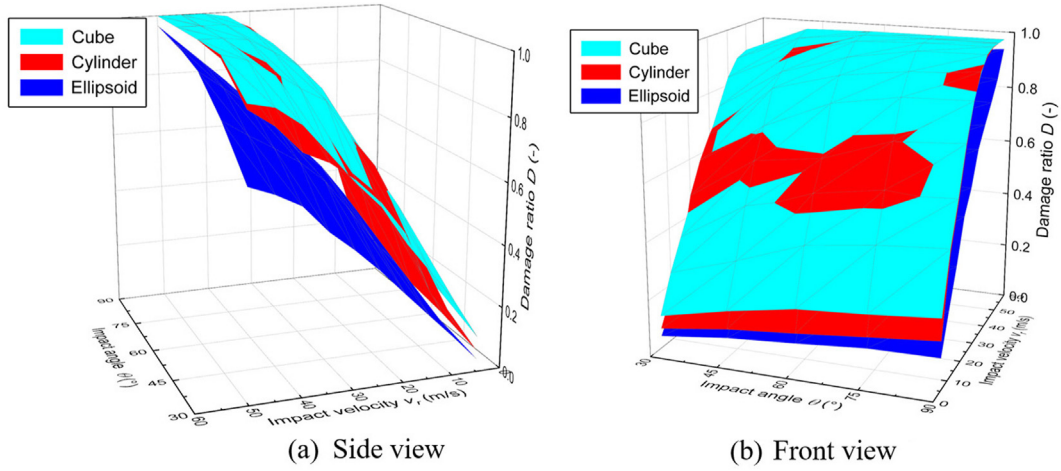


Fig. 8. Damage ratios for three particle shapes. (a) Side view (b) Front view.

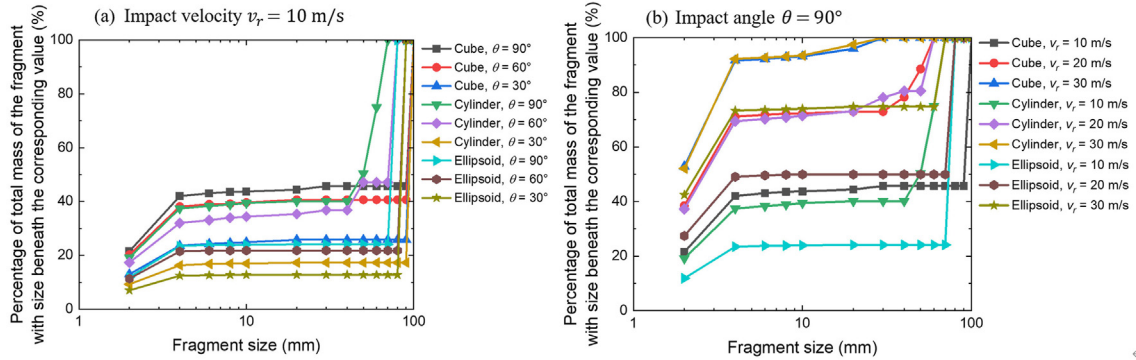


Fig. 9. Particle size distribution (PSD) at the final stage of the impact.

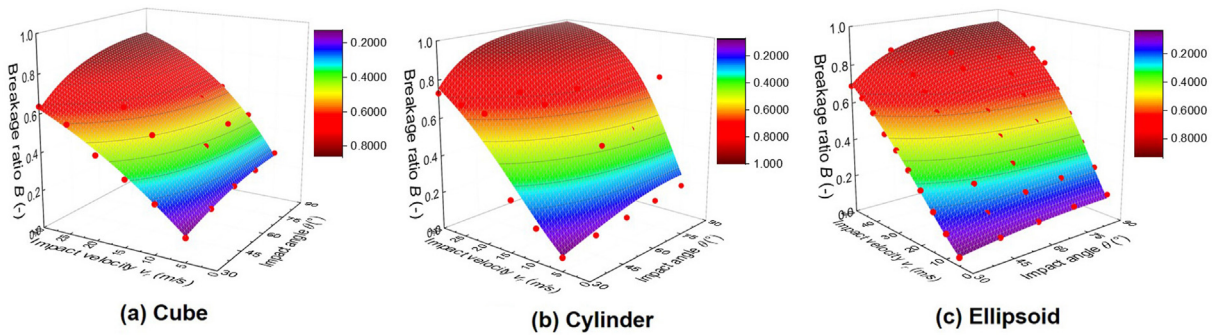


Fig. 10. Unified breakage master surface of breakage ratio.

superellipsoid, with the only difference of roundness. From ellipsoid to cylinder, the first roundness  $\varepsilon_1$  keeps 1.0 whilst the second roundness  $\varepsilon_2$  decreases from 1.0 to positive infinite small (Soltanbeigi et al., 2021); from cylinder to cube, the first roundness  $\varepsilon_1$  decreases from 1.0 to positive infinite small whilst the second roundness  $\varepsilon_2$  keeps the positive infinite small. Therefore,  $\xi$  and  $\gamma$  decrease with  $\varepsilon_2$  while  $m$  increases with decreased  $\varepsilon_2$ , from comparison of ellipsoid and cylinder;  $\xi$  and  $\gamma$  increase with decreased  $\varepsilon_1$  while  $m$  decreases with  $\varepsilon_1$ , from comparison of cylinder and cube. There might be quantitative links between  $\xi$ ,  $\gamma$ ,  $m$  and roundness

parameters  $\varepsilon_1, \varepsilon_2$ , which needs further investigation in the future. In addition, according to the previous study (Wang et al., 2022),  $\xi$  refers to tangential behaviour and should not be negative. However, for cylinder, the mean of fitted  $\xi$  is below zero, which is unphysical. Comparing subfigures in Fig. 10, the fitting of master curve for cylinder is the most suboptimal. As  $\xi$  refers to tangential behaviour, and the three types of agglomerates have different instant contact area during oblique impact, it is assumed that the instant contact area may have an effect during oblique impact and the master curve model may be upgraded considering the effect in the future work.

**Table 4**  
Fitted parameters.

Description	Value
Cube	
Tangential contribution factor $\xi$	$0.13755 \pm 0.09609$
Velocity normalisation factor $\gamma$	$16.07175 \pm 0.38260$
Velocity exponent $m$	$1.08669 \pm 0.03391$
Cylinder	
Tangential contribution factor $\xi$	$-0.08600 \pm 0.25903$
Velocity normalisation factor $\gamma$	$11.66754 \pm 0.77681$
Velocity exponent $m$	$1.60526 \pm 0.17135$
Ellipsoid	
Tangential contribution factor $\xi$	$0.40447 \pm 0.04067$
Velocity normalisation factor $\gamma$	$25.15075 \pm 0.18234$
Velocity exponent $m$	$1.43027 \pm 0.01594$

#### 4.6. Discussion on constituent sphere resolution

The constituent sphere resolution, as well as the bond parameters/properties, may affect the master curve. When the size of agglomerate remains unchanged while the size of constituent spheres decreases, i.e. the agglomerate contains more constituent spheres, the coarse graining approach (Nasato et al., 2015) can be adopted giving the same mechanical behaviour (including breakage) by combining several constituent spheres to relatively larger particles and changing the contact properties accordingly as the coordination number has changed. In this case, the master curve model can still predict the breakage of the agglomerate, though the fitting parameters of the curve may change with bond properties. However, when the size of agglomerate decreases while the size of constituent spheres remains unchanged, i.e. the agglomerate contains fewer constituent spheres, the boundary effect will enlarge within the agglomerate and the simulated mechanical behaviour of the agglomerate may not be true. Therefore, sufficient constituent spheres are needed within the agglomerate to control its boundary effect and properly represent its mechanical behaviour. O'Sullivan (O'Sullivan, 2011) discussed this issue and suggested the size of the agglomerate should be at least 10–20 times the largest constituent sphere size to ensure enough constituent spheres with the number of at least 1000–8000. The agglomerates in this article all contain around 18,000 constituent spheres, which is appropriate.

## 5. Conclusions

In this article, DEM modelling of nonspherical particle breakage under oblique impact conditions was carried out using a DEM bonded contact model. Three particle shapes, cubical, ellipsoidal and cylindrical, are considered where particle shape plays a critical role in the breakage pattern. The damage ratio, as a function of the number of broken bonds, is converted to breakage ratio, a function of fragment size distribution. This conversion serves to establish the relationship between microscopic and macroscopic breakage properties. To that end, a Breadth-First Search Algorithm was developed to elaborate the bonding clusters following impact breakage. The effect of impact angle is specifically studied for nonspherical particle impact breakage and the tangential velocity component becomes increasingly important at shallow impact angles. In particular, the breakage ratio with varied impact angles is found to deviate as a function of either impact velocity or normal velocity component. The equivalent velocity model exclusive to oblique impact is proposed in a recently developed breakage model. Using the equivalent velocity combined with DEM, unified

breakage master surfaces are theoretically constructed for various particle shapes. It is noted that in this article the bond model is adopted to model fracture and breakage in macro scale; particle breakage mechanism at nanoscale may differ from this prediction due to constitutive model inapplicability.

## Declaration of interest

The authors declare that they have no known competing financial interests or personal relationships that could have appeared to influence the work reported in this article.

## Acknowledgement

The authors gratefully acknowledge the financial support from National Natural Science Foundation of China Excellent Young Scientists Fund Program (Overseas) (grant No. YQ2023-22), Shandong Excellent Young Scientists Fund Program (Overseas) (grant No. 2022HWYQ-020), Shenzhen Science and Technology Program (grant No. RCBS20200714114910354, JCYJ20220530141016036 and GJHZ20200731095006019).

## References

- Andrade, J. E., Lim, K.-W., Avila, C. F., & Vlahinić, I. (2012). Granular element method for computational particle mechanics. *Computer Methods in Applied Mechanics and Engineering*, 241, 262–274.
- Brown, N. J., Chen, J.-F., & Ooi, J. Y. (2014). A bond model for DEM simulation of cementitious materials and deformable structures. *Granular Matter*, 16, 299–311.
- Capozza, R., & Hanley, K. J. (2021). A hierarchical, spherical harmonic-based approach to simulate abradable, irregularly shaped particles in DEM. *Powder Technology*, 378, 528–537.
- Chen, X., Wang, L. G., Meng, F., & Luo, Z.-H. (2021). Physics-informed deep learning for modelling particle aggregation and breakage processes. *Chemical Engineering Journal*, 426, 131220.
- Chen, X., Wang, L. G., & Ooi, J. Y. (2020). A DEM-PBM multiscale coupling approach for the prediction of an impact pin mill. *Powder Technology*, 366, 408–419.
- Cheong, Y., Salman, A., & Hounslow, M. (2003). Effect of impact angle and velocity on the fragment size distribution of glass spheres. *Powder Technology*, 138(2–3), 189–200.
- DCS Computing GmbH. (2020). *Aspherix -DEM*. <https://www.aspherix-dem.com/>.
- Ge, R., Ghadiri, M., Bonakdar, T., & Hapgood, K. (2017). 3D printed agglomerates for granule breakage tests. *Powder Technology*, 306, 103–112.
- Ge, R., Ghadiri, M., Bonakdar, T., Zheng, Q., Zhou, Z., Larson, I., & Hapgood, K. (2020). Deformation of 3D printed agglomerates: Multiscale experimental tests and DEM simulation. *Chemical Engineering Science*, 217, 115526.
- Ge, R., Ghadiri, M., Bonakdar, T., Zhou, Z., Larson, I., & Hapgood, K. (2018). Experimental study of the deformation and breakage of 3D printed agglomerates: Effects of packing density and inter-particle bond strength. *Powder Technology*, 340, 299–310.
- Ge, R., Wang, L., & Zhou, Z. (2019). DEM analysis of compression breakage of 3D printed agglomerates with different structures. *Powder Technology*, 356, 1045–1058.
- Jiménez-Herrera, N., Barrios, G. K., & Tavares, L. M. (2018). Comparison of breakage models in DEM in simulating impact on particle beds. *Advanced Powder Technology*, 29(3), 692–706.
- Kafui, K., & Thornton, C. (2000). Numerical simulations of impact breakage of a spherical crystalline agglomerate. *Powder Technology*, 109(1–3), 113–132.
- Kh, A. B., Mirghasemi, A., & Mohammadi, S. (2011). Numerical simulation of particle breakage of angular particles using combined DEM and FEM. *Powder Technology*, 205(1–3), 15–29.
- Liu, L., Kafui, K., & Thornton, C. (2010). Impact breakage of spherical, cuboidal and cylindrical agglomerates. *Powder Technology*, 199(2), 189–196.
- Liu, Z., Ma, H., & Zhao, Y. (2021). Comparative study of discrete element modeling of tablets using multi-spheres, multi-super-ellipsoids, and polyhedrons. *Powder Technology*, 390, 34–49.
- Lu, G., Third, J., & Müller, C. (2015). Discrete element models for non-spherical particle systems: From theoretical developments to applications. *Chemical Engineering Science*, 127, 425–465.
- Mishra, B. (2000). Monte Carlo simulation of particle breakage process during grinding. *Powder Technology*, 110(3), 246–252.
- Monteiro Azevedo, N., Candeias, M., & Gouveia, F. (2015). A rigid particle model for rock fracture following the voronoi tessellation of the grain structure: Formulation and validation. *Rock Mechanics and Rock Engineering*, 48, 535–557.



- Moré, J. J. (2006). *The Levenberg-Marquardt algorithm: Implementation and theory, numerical analysis: Proceedings of the Biennial Conference Held at Dundee* (pp. 105–116). Springer. June 28–July 1, 1977.
- Moreno-Atanasio, R., & Ghadiri, M. (2006). Mechanistic analysis and computer simulation of impact breakage of agglomerates: Effect of surface energy. *Chemical Engineering Science*, 61(8), 2476–2481.
- Nasato, D. S., Goniva, C., Pirker, S., & Kloss, C. (2015). Coarse graining for large-scale DEM simulations of particle flow—an investigation on contact and cohesion models. *Procedia Engineering*, 102, 1484–1490.
- O'Sullivan, C. (2011). *Particulate discrete element modelling: A geomechanics perspective*. CRC Press.
- Orozco, L. F., Delenne, J.-Y., Sornay, P., & Radjai, F. (2019). Discrete-element model for dynamic fracture of a single particle. *International Journal of Solids and Structures*, 166, 47–56.
- Otsubo, M., O'Sullivan, C., & Shire, T. (2017). Empirical assessment of the critical time increment in explicit particulate discrete element method simulations. *Computers and Geotechnics*, 86, 67–79.
- Peng, D., Burns, S. J., & Hanley, K. J. (2021). Critical time step for discrete element method simulations of convex particles with central symmetry. *International Journal for Numerical Methods in Engineering*, 122(4), 919–933.
- Podlozhnyuk, A., Pirker, S., & Kloss, C. (2017). Efficient implementation of superquadric particles in Discrete Element Method within an open-source framework. *Computational Particle Mechanics*, 4, 101–118.
- Qin, C., Ma, C., Li, L., Sun, X., Liu, Z., & Sun, Z. (2023). Development and application of an intelligent robot for rock mass structure detection: A case study of letuan tunnel in Shandong, China. *International Journal of Rock Mechanics and Mining Sciences*, 169, 105419.
- Salman, A., Gorham, D., & Verba, A. (1995). A study of solid particle failure under normal and oblique impact. *Wear*, 186, 92–98.
- Shang, J. (2022). Stress path constraints on veined rock deformation. *Rock Mechanics Bulletin*, 1(1), 100001.
- Soltanbeigi, B., Podlozhnyuk, A., Kloss, C., Pirker, S., Ooi, J. Y., & Papanicolopoulos, S.-A. (2021). Influence of various DEM shape representation methods on packing and shearing of granular assemblies. *Granular Matter*, 23, 1–16.
- Soltanbeigi, B., Podlozhnyuk, A., Papanicolopoulos, S.-A., Kloss, C., Pirker, S., & Ooi, J. Y. (2018). DEM study of mechanical characteristics of multi-spherical and superquadric particles at micro and macro scales. *Powder Technology*, 329, 288–303.
- Subero, J., & Ghadiri, M. (2001). Breakage patterns of agglomerates. *Powder Technology*, 120(3), 232–243.
- Thakur, S. C., Ooi, J. Y., & Ahmadian, H. (2016). Scaling of discrete element model parameters for cohesionless and cohesive solid. *Powder Technology*, 293, 130–137.
- Thornton, C., & Liu, L. (2004). How do agglomerates break? *Powder Technology*, 143, 110–116.
- Wang, L. G., Chen, J.-F., & Ooi, J. Y. (2021). A breakage model for particulate solids under impact loading. *Powder Technology*, 394, 669–684.
- Wang, L. G., Ge, R., & Chen, X. (2022). Establishing an oblique impact breakage master curve using a DEM bonded contact model. *Computers and Geotechnics*, 145, 104668.
- Wang, L. G., Ge, R., Chen, X., Zhou, R., & Chen, H.-M. (2021). Multiscale digital twin for particle breakage in milling: From nanoindentation to population balance model. *Powder Technology*, 386, 247–261.
- Yang, W., Lv, X., Wang, L., Peng, D., & Chen, X. (2023). A DEM–CFD coupling method for modelling two-hole synchronous hydraulic fracturing. *Geomechanics and Geophysics for Geo-Energy and Geo-Resources*, 9(1), 6.
- Ye, Y., Zeng, Y., Cheng, S., Sun, H., & Chen, X. (2021). Numerical investigation of rock sphere breakage upon oblique impact: Effect of the contact friction coefficient and impact angle. *Computers and Geotechnics*, 136, 104207.
- Yuregir, K., Ghadiri, M., & Clift, R. (1986). Observations on impact attrition of granular solids. *Powder Technology*, 49(1), 53–57.
- Zeng, Y., Jia, F., Xiao, Y., Han, Y., & Meng, X. (2019). Discrete element method modelling of impact breakage of ellipsoidal agglomerate. *Powder Technology*, 346, 57–69.
- Zheng, K., Du, C., Li, J., Qiu, B., Fu, L., & Dong, J. (2015). Numerical simulation of the impact-breakage behavior of non-spherical agglomerates. *Powder Technology*, 286, 582–591.